JAMES | Journal of Advances in Modeling Earth Systems

RESEARCH ARTICLE
10.1029/2019MS001625

Sensitivity of Limited Area Atmospheric Simulations to Lateral Boundary Conditions in Idealized Experiments

Nora Leps[1], **Jennifer Brauch**[2], **and Bodo Ahrens**[1]

[1]Institute for Atmospheric and Environmental Sciences, Goethe University, Frankfurt am Main, Germany, [2]Deutscher Wetterdienst, Offenbach am Main, Germany

Key Points:
- Lateral boundary conditions were tested in an idealized atmospheric limited area model
- Dominance of driving data quality over temporal update frequency and lateral boundary scheme was found
- There was no beneficial effect of spectral nudging in idealized limited area simulations

Correspondence to:
N. Leps,
leps@iau.uni-frankfurt.de

Citation:
Leps, N., Brauch, J., & Ahrens, B. (2019). Sensitivity of limited area atmospheric simulations to lateral boundary conditions in idealized experiments. *Journal of Advances in Modeling Earth Systems*, *11*, 2694–2707. https://doi.org/10.1029/2019MS001625

Received 18 JAN 2019
Accepted 11 JUL 2019
Accepted article online 20 JUL 2019
Published online 19 AUG 2019

Abstract The goal of limited area models (LAMs) is to downscale coarse-gridded general circulation model output to represent small-scale features of weather and climate. The LAM needs information from the driving coarse-gridded model passing through its lateral boundaries. The treatment of this information transfer causes inconsistencies between driving and nested models and, subsequently, issues in regional weather and climate simulations. This work examines errors arising from choices taken by the modeler (temporal update frequency of boundary data, spatial resolution jump, and numerical lateral boundary formulation) systematically in an idealized simulation environment. So-called Big-Brother Experiments were performed with the LAM COSMO-CLM (0.11° grid spacing). A baroclinic wave in a zonal channel was simulated over flat terrain with and without a Gaussian hill. The results reveal that the quality of the driving data, here represented by simulations only differing from the LAM simulations by reduced spatial resolution, dominates the performance of the nested model. Consequently, at the simulated mesoscale, the performance of the nested small-scale model simulations is weakly sensitive to the numerical lateral boundary formulation (Davies relaxation or the newly implemented, computationally less demanding Mesinger Eta-model formulation). The performance sensitivity to boundary update frequency and resolution jump is small when at least 6-hourly updates and a resolution jump factor of maximally six is used. Gaussian hill LAM simulations illustrated the strength of downscaling; they can represent small-scale features missing in the coarse-scale driving simulations. In the idealized simulation experiments, spectral nudging is not advisable as it imprints the driving models deficits on the nested simulation.

1. Introduction

General circulation models (GCMs) can simulate global-scale climate processes (e.g., Hargreaves, 2010; Räisänen, 2007) despite their limitations and uncertainties. There is, however, a demand for high-resolution information on local processes (in weather or past and future climate). Dynamical downscaling adds this additional small-scale information to predictions and projections (e.g., Giorgi et al., 2009; Mieruch et al., 2014). The most common approach in climate modeling is one-way nesting: coarse-scale data from a reanalysis or GCM simulation drives a higher resolved limited area model (LAM), which then acts as a regional climate model (RCM; Rummukainen, 2010). It can simulate small-scale atmospheric processes not resolved by the GCM and represent land surface characteristics and topography more realistically (e.g., Paeth & Mannig, 2013). The GCM provides initial and boundary conditions for the RCM, including lateral atmospheric boundary conditions (LBCs), upper and lower boundary conditions (which can be given by the driving model or via a land surface or ocean model, e.g., Pham et al., 2018). Here, we focus on the LBCs.

Denis, Laprise, et al. (2002) list and explain several sources of LBC-related errors in LAMs based on Warner et al., 1997 (1997, who gave some guidelines for handling LBC problems in numerical weather prediction) and Giorgi and Mearns (1999). Some of those are caused by the inherent difference between LAM and GCM and some by features of the LAMs themselves. In the past decades, several studies have been conducted to tackle these issues.

In RCM applications, Becker et al. (2015) described large-scale secondary circulations in regional simulations compared to coarse input data, caused by the different representation of topography in RCM and GCM and dependent on the choice of the RCM domain. Matte et al. (2017) investigated the spatial spin-up that is necessary for RCMs to develop fine scales from the lateral boundary data. Additionally, RCMs usually use different physical parameterizations, causing inconsistencies in the model solution.

GCM output generally has a lower spatial resolution compared to the LAM. Thus, a vertical and horizontal interpolation is necessary, which leads to interpolation errors. Køltzow et al. (2008) investigated how the quality of the driving data and the size of the integration domain influences RCM simulations. When the regional domain is too small, the RCM has problems to correctly simulate large scale patterns. The larger it is, the more it is able to add features determined by local forcing.

Two factors determined by the spatial resolution and temporal availability of the driving data are the spatial resolution jump, quantified by the ratio of grid spacings of nested and driving model, and the temporal update frequency. Typical global simulations today, such as those generated in CMIP5 (Taylor et al., 2012), have grid spacings of 0.5° to 4° , with the majority ranging from 1° to 3°. Current RCMs, such as those used for the CORDEX (Coordinated REgional Climate Downscaling Experiment; e.g., Giorgi et al., 2009), use grid spacings of 0.44° and smaller, which results in spatial resolution jumps of roughly 5 to 10. Beck et al. (2004) tested nesting strategies with an RCM of 12-km grid spacing, which is common for current RCMs, and concluded that a spatial resolution jump of 10 is acceptable for downscaling over complex terrain; no intermediate nesting is necessary. With future developments toward GCMs of 25-km grid spacing (Roberts et al., 2018), resolutions in RCMs also increase (e.g., toward convection-permitting regional climate simulations), which inhibits a reduction of spatial resolution jumps. Brisson et al. (2015) evaluated the influence of nesting strategies in a convection permitting RCM driven by reanalysis data with grid spacing of 0.75° and conclude that one intermediate nesting step is necessary but also sufficient. The driving data for RCMs is usually provided every 6 hr and then linearly interpolated to model time steps of well below 1 hr. In future, however, boundary data might be available hourly (e.g., ECMWF ERA5 reanalysis; Hersbach et al., 2018). Denis et al. (2003) and Antic et al. (2006) evaluated the two issues with an RCM (grid spacing of 45 km), concluding that a spatial resolution jump of 12 and 12-hourly updates are adequate, but results can improve with 6-hourly updates.

A further issue is the mathematical and numerical formulation of the LBCs. LAMs base on atmospheric dynamics following physical laws. These are formulated mathematically as partial differential equations, which need LBCs. The equations are solved numerically, and many efforts have been made to formulate these LBCs optimally for several reduced systems of equations. Examples are listed in the review by McDonald (1999); however, for fully nonhydrostatic equations the optimal solution is not known. Recently, some efforts have been made to formulate well-posed boundary conditions for the Navier-Stokes equations (Nordström, 2017); this approach might also be used in RCMs in the future. McDonald (2002) stated that good LBCs have to be transparent. Thus, the LBCs have to fulfil the task of (a) letting small-scale information generated by the LAM leave the domain without reflection at the outflow boundary, where there is a mismatch to the GCM boundary data that lacks small-scale features, and (b) transferring large-scale information provided by the GCM into the LAM domain.

Most LAMs use the Davies relaxation (DR) approach (Davies, 1976). Here, all variables are prescribed at all lateral boundaries, which means the problem is over-specified (too much information is given at the LBCs; McDonald, 1999). A sponge zone is introduced to buffer any spurious noise developing at the lateral boundary, where the internal LAM solution is relaxed toward the driving data. An alternative approach was introduced by Mesinger (1977) for the Eta-model based on Sundström (1973). This Mesinger Eta-model LBC scheme (here, abbreviated ME) prescribes less information, thus avoiding overspecification of the variables at the lateral boundaries and giving the LAM more freedom to develop less restricted by the driving data. The variables are prescribed at one row at the boundary points except at the outflow points, where the tangential velocity component is extrapolated from the interior solution. The two schemes have been compared in a full model by Veljovic et al. (2010) and Mesinger and Veljovic (2013). They encourage the use of the ME scheme but have only tested it on the not so common Arakawa E-grid.

An often used technique to reduce inconsistencies between RCM and driving data is spectral nudging (von Storch et al., 2000), which can also reduce the issues developing due to LBC treatment (Omrani et al., 2012). In spectral nudging, the large scales of the model fields of the RCM are nudged toward the driving fields. This approach can also be seen critically (e.g., Mesinger & Veljovic, 2017), as it inhibits any improvement of the large scales by the LAM.

This work aims at assessing the errors arising from the LAM side. Systematic idealized experiments with several combinations of temporal update frequency and spatial resolution jump are performed with the RCM COSMO model in Climate Mode (COSMO-CLM, e.g., Rockel et al., 2008). In this idealized setting, it is easier

to evaluate the nesting errors than in a full model simulation. We use a higher resolution (grid distances 0.11°) than in most previous studies. We introduce ME in COSMO-CLM and test the two LBC schemes on the C grid, which is more common in RCMs than the E grid and where it has not been used yet. With the previous studies and current and future simulations in mind, we answer the following questions:

1. How do resolution jumps in space and temporal update frequency impact the representation of a typical midlatitude atmospheric phenomenon in an idealized RCM and what are useful ranges for both?
2. What is the impact of using different LBC schemes in comparison to errors caused by resolution jumps in space and time, and is there a clear advantage of one of the two investigated LBC schemes (DR and ME) over the other?
3. How does spectral nudging impact the simulations?

To answer these questions, we developed idealized experiments. The advantage of these is that the problem is reduced to an easy-to-understand setting, only considering dynamics and LBC settings of the model and omitting physical parameterizations. The test setup is based on the "Big-Brother-Experiment" (BBE) approach (Denis, Laprise, et al., 2002), where inconsistencies due to different model grids and physics parameterizaions can be ruled out. We use a synoptic-scale phenomenon for the experiments, a baroclinic wave (typical spatial scale of 2,000 to 10,000 km) with pressure systems and fronts (typical spatial scale of 200 to 2,000 km), ranging at the transition between mesoscale and macroscale (Orlanski, 1975) and usually well represented in RCMs. For this, COSMO-CLM is set up as a channel model, based on Ullrich et al. (2015).

2. Method, Model, and Experiments

2.1. Method—The Big-Brother-Experiment Protocol

We use an experiment setup closely following the Big-Brother-Experiment protocol described by Denis, Laprise, et al. (2002). First, a simulation on a high-resolution grid is performed. Ideally, it would cover the whole globe, but for practical reasons, it is usually calculated on a large regional domain and is called "Big Brother" (henceforward *BB*). The simulation data serves as the reference and the basis for the initial and boundary conditions of a nested simulation on a smaller domain (the so-called "Little Brother," *LB*). The *LB* simulation uses the same high-resolution grid, such that it can directly be compared to the reference. The boundary data, however, is modified in between. A discrete cosine transform filter (see Appendix A for details) is applied to the *BB* output data to remove small-scale features with wavelengths below a specified threshold. This filtered data mimics "real" coarse-resolution driving data; however, it is still given on the high-resolution grid to exclude interpolation errors and is called "Filtered Brother" *FB*. Thus, different resolution jumps can be created artificially, and different LBC settings and schemes can be tested by comparing the *LB* output to the reference *BB* output.

The advantage of this strategy is that the errors occurring in LAMs because of reasons other than the LBCs can be ruled out, as both the generation of driving data and the nested simulation use the same model.

In this work, not only the classical BBE approach is used, but two additional modified setups. First, the *BB* reference output is directly used as initial and boundary data for the *LB* to test the influence of different temporal update frequencies. Second, additional simulations are performed on the *BB* domain with lower resolution, to create spatial resolution jumps as in full GCM and RCM simulations (this "Coarse Brother" is called *CB*).

2.2. Model—COSMO-CLM

Simulations were performed with COSMO-CLM, a nonhydrostatic RCM (e.g., Rockel et al., 2008). We used version COSMO5.0-CLM7 and the preprocessor INT2LM2.0-CLM4 for boundary data generation. For the idealized experiments, the physical parameterizaions were switched off; there was no diurnal cycle of radiation, and a free-slip lower boundary condition and the atmosphere was considered to be dry. A useful feature of COSMO-CLM is the possibility to simulate idealized test cases (Blahak, 2015), where simulations with artificial initial and boundary conditions over artificial topography are possible. The initial conditions for *BB* simulations were that of the newly implemented baroclinic wave test case based on Ullrich et al. (2015). The *LB* simulations used two different LBC schemes: the default DR and the newly implemented ME (details in sections 2.2.1 and 2.2.2). *BB* and *LB* simulations were performed with grid spacing $\Delta\text{lon} = \Delta\text{lat} = 0.11°$, as in, for example, the EURO-CORDEX project (https://www.euro-cordex.net).

2.2.1. DR Scheme in COSMO-CLM

The DR has been developed for limited area prediction models (Davies, 1976) and since then has also been used in RCMs (Marbaix et al., 2003). All variables are prescribed at all boundaries, and a relaxation zone is introduced to buffer differences between driving and nested model fields because of overspecification and model inconsistencies. In this zone, the interior model fields are relaxed toward the driving model fields.

COSMO-CLM uses DR as default LBC scheme (Doms & Baldauf, 2015). It is performed as part of the time integration, with a relaxation term added to all the prognostic equations at each time step, resulting in the relaxation equation:

$$\psi_2 = \psi_1 - \alpha_b \left(\psi_1 - \psi_b\right) \tag{1}$$

Here, ψ stands for the 3-D fields of the prognostic variables (temperature, three wind components, air pressure), $\psi_{1,2}$ before and after relaxation and the driving fields ψ_b. The 2-D field $\alpha_b(d)$, the attenuation function, depends on the distance d to the boundary. At the three outermost rows, $\alpha_b = 1$, when $d >$ width of relaxation zone, $\alpha_b = 0$. In between it follows an exponential decay function. In our experiments the relaxation zone width is 150 km, corresponding to the recommendations of Schättler et al., 2016 (2016; 10 to 15 times the grid spacing and less than 0.25 times the domain size).

2.2.2. Mesinger Eta-Model LBC Scheme in COSMO-CLM

Mesinger (1977) developed this approach for the Eta model. It is based on a suggestion by Sundström (1973), who recommended for hydrostatic models to prescribe tangential velocity at inflow boundaries only and prescribe all other variables at all boundaries to avoid overspecification.

We implemented this alternative way of treating LBCs in the COSMO-CLM model based on the description in Black (1988). Originally it was written for an Arakawa-E grid and has been adapted to the COSMO-CLM Arakawa-C grid. This adaption and the use of a different advection scheme made the following modifications necessary. First, all prognostic variables are prescribed at the three outermost rows of the regional domain. Originally, they are prescribed at only one row; however, COSMO-CLM uses a third-order horizontal advection scheme and needs three prescribed grid points at the boundary. In the fifth row, the normal component of the horizontal wind is checked. If the grid point is an outflow point, the tangential horizontal wind component is extrapolated to the three outermost rows (instead of only one row) and thus not prescribed by the driving data. Finally, the values of all variables at the fourth row (instead of the second row in Black, 1988) are averaged from the adjoining points as a buffer between the interior and the boundary fields.

2.2.3. Spectral Nudging

Spectral nudging is a technique where the large scales of the RCM fields are nudged toward the large-scale fields of the GCM (Omrani et al., 2012; von Storch et al., 2000). The purpose of spectral nudging is to keep the large scales of the nested model closer to those of the driving model. Inconsistencies at the boundary can be reduced as the nested model does not drift away from the driving solution. In most experiments here, spectral nudging is switched off except for some, to investigate its effect on the simulations. If activated, the COSMO-CLM default settings for spectral nudging are used: Meridional and zonal wind are nudged above a pressure level of 850 hPa at every time step.

2.3. Experiments

"Big Brother" (*BB*), "filtered Driving Brother" (*FB*), "coarse Driving Brother" (*CB*), and "Little Brother" (*LB*) simulations used the same model settings (except for the domain size/location and the LBC modifications in *LB* simulations) and the same grid (except for *CB* with larger grid spacing). Two model setups were performed: one with flat terrain and one with a Gaussian hill. The hill was represented differently in the simulations due to different spatial resolutions, which introduced an additional inconsistency of the fields at the *LB* lateral boundaries.

2.3.1. The Baroclinic Wave Test Case Experiment

The baroclinic wave test case was originally designed to assess and compare dry dynamical cores of GCMs (Jablonowski & Williamson, 2006) and is completely determined by the analytic initial conditions. The background flow is a hydrostatically and geostrophically balanced steady-state jet stream in the northern midlatitudes. A perturbation in the zonal wind field is added that triggers the baroclinic wave, which develops over several days. Ullrich et al. (2015) formulated it for regional applications and presented analytic initial conditions for testing dry 3-D models. The RCMs were set up as channel models around the northern midlatitudes on an f or β plane with flat terrain. The simulation domain represents a tangential plane around

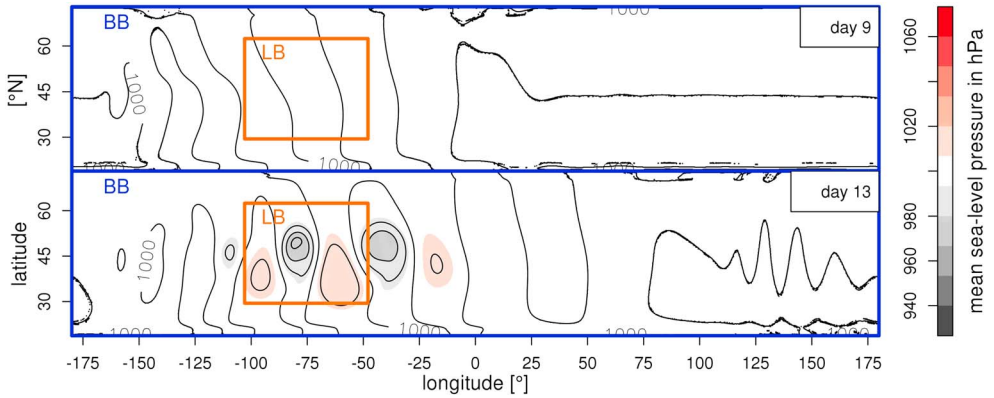

Figure 1. Mean sea level pressure of the baroclinic wave over flat terrain in the *BB* simulation (contour interval: 10 hPa). The top and bottom panels show forecast Days 9 and 13, respectively. The blue boxes indicate the *BB* domain, orange boxes the *LB* domain. *BB* = Big Brother; *LB* = Little Brother.

the earth at a fixed latitude φ_0 with either a constant Coriolis parameter (f plane) or a Coriolis parameter linearly dependent on latitude (β plane). The zonal boundary conditions were periodic, while values were fixed to the initial state at the meridional boundaries. For this work, the f plane version has been implemented in COSMO-CLM (Coriolis parameter $f = 2\Omega \sin(\varphi_0)$, Ω being the rotation rate of the Earth). Here, we used northern midlatitudes, $\varphi_0 = 45°$ and vertical Gal-Chen height coordinates with 42 model levels.

We also used a modification of the baroclinic wave test case, with a Gaussian hill added to the terrain which introduced an additional perturbation of the flow.

2.3.2. *BB*, *FB*, and *CB* simulations

The *BB* simulations, starting at day 00, hour 00 with initial conditions of the baroclinic wave over flat terrain or with the hill, respectively, covered 17 days. Ullrich et al. (2015) advised to run the simulations for at least 15 days. The pressure systems that accompanied the wave became distinct after about 10 days, and the solution started to degenerate after day 17 when the pressure systems reach the northern and southern boundaries of the *BB* domain, where fixed values constrain the simulation. The domain covered a channel around the Earth in midlatitudes (about $40,000 \times 6,000$ km^2, southwest corner at 179.93°W and 18.88°N (blue box in Figures 1 and 2). If present, the Gaussian hill was situated at 87.53°W and 45.28°N and had a height of 750 m and half width of 50 km in the reference simulation (*BB*). Additionally to *BB*, three *CB* simulations were performed with coarser grid spacings of 0.33°, 0.66°, and 1.10°. The hill was flattened in these coarse simulations, as would real topography in a coarse-scale driving model, hill properties were chosen such that the hill had approximately the same volume in all simulations. Finally, the output of *BB* was filtered to *FB* with the technique presented in section 2.1 to represent similar spatial resolution jumps as the *CB* simulations (for details, see Appendix A). Simulation properties are given in Table 1.

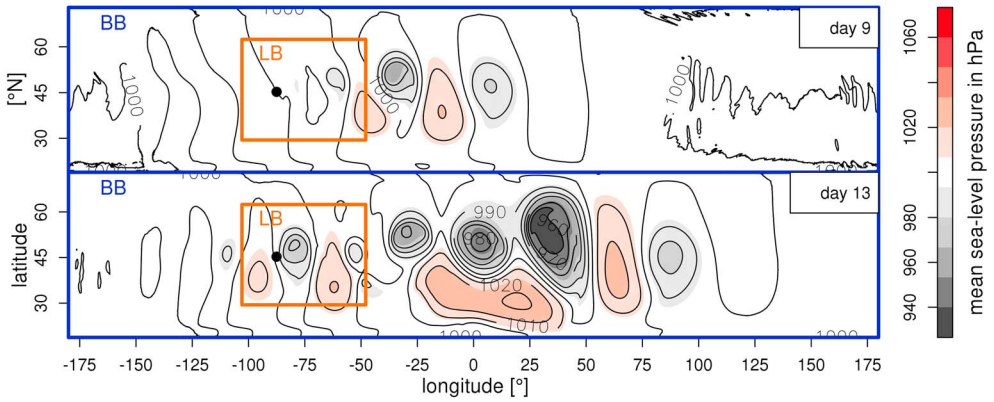

Figure 2. Same as Figure 1 with Gaussian hill (position indicated by black dot). *BB* = Big Brother; *LB* = Little Brother.

Table 1
Properties of BB and LB Domains and Simulations

Name	Δlongitude, Δlatitude	Nx	Ny	dt
BB	0.11° ≈ 12 km	3,272	492	90 s
CB	0.33° ≈ 36 km	1,091	164	180 s
	0.66° ≈ 72 km	545	82	360 s
	1.10° ≈ 120 km	328	50	450 s
FB	0.11° ≈ 12 km	3,272	492	90 s
LB	0.11° ≈ 12 km	501	301	90 s

Note. *BB* = Big Brother; *LB* = Little Brother; *CB* = Coarse Brother; *FB* = Filtered Brother.

2.3.3. *LB* Simulations

All the following *LB* simulations were done twice, once with flat terrain and once with the Gaussian hill. The domain was approximately $6{,}105 \times 3{,}663\ km^2$, close to the size of the EURO-CORDEX domain, and centered around 75.43°E and 45.94°N (orange box in Figures 1 and 2), just downstream of the area of cyclogenesis.

Temporal update frequency (U) and spatial resolution jump (J) are defined as in Denis et al. (2003) and Antic et al. (2006). U is the number of lateral boundary updates per day. The model dynamics and numerics need lateral boundary values at every model time step, so the values were linearly interpolated between the update times, as is done operationally in LAMs. J is the ratio of resolutions of *LB* and driving data, and thus the inverse ratio of their grid spacing. When *LB*s are driven by *BB* directly, $J = \frac{\Delta\mathrm{lon}(BB)}{\Delta\mathrm{lon}(LB)} = 1$, when driven by *CB*, $J = \frac{\Delta\mathrm{lon}(CB)}{\Delta\mathrm{lon}(LB)}$. The *FB* simulations are filtered to the desired resolution jump as described in detail in Appendix A.

The sets of test simulations are listed below. Unless indicated otherwise, they were done with DR and with spectral nudging switched off.

1. *Temporal update frequency only:* Driving data *BB*, fixed $J = 1$, $U \epsilon \{24, 8, 4, 2\}$
2. *Temporal update frequency and spatial resolution jump:* Driving data from *CB* and *FB*, U and J varied ($U \epsilon \{24, 8, 4, 2\}$ and $J \epsilon \{3, 6, 10\}$)
3. *Different LBC schemes DR and ME*
4. *Spectral nudging*

The simulations for tests 3 and 4 are (1) the setting with lowest jumps in space and time: *LB* driven by *BB* hourly $(U, J) = (24, 1)$, and (2) three combinations of typically used jumps: *LB* driven by *CB* and *FB*, respectively, with $(U, J) \epsilon \{(8, 3), (4, 6), (2, 10)\}$.

2.4. Evaluation

Results of the experiments are evaluated using quarter-hourly mean sea level pressure *MSLP*. For comparing the different *CB*/*FB* and *LB* simulations to the reference *BB*, we used the time-dependent root-mean-square error (RMSE) over the *LB* domain, based on equation (16) in Jablonowski and Williamson (2006):

$$RMSE(t) \approx \sqrt{\frac{\Sigma_{i=1}^{Nx}\Sigma_{j=1}^{Ny}\left\{MSLP(\lambda_i, \varphi_j, t) - MSLP_{BB}(\lambda_i, \varphi_j, t)\right\}^2 w_j}{\Sigma_{i=1}^{Nx}\Sigma_{j=1}^{Ny} w_j}} \tag{2}$$

where λ_i and φ_j are latitudes and longitudes of the grid points, respectively, and $w_j = |\sin(\varphi_{j+1/2}) - \sin(\varphi_{j-1/2})|$ a weighting factor. The area of the relaxation zones is excluded in the evaluation, and the *CB* fields have been mapped bilinearly to the *BB* grid for these calculations.

Next to time series we take the temporal means of $RMSE(t)$ and root-mean-square skill scores, based on the evaluation methods of the MiKlip project, https://www-miklip.dkrz.de/about/murcss/. It compares means of $RMSE(t)$ of simulation *sim* to that of a reference simulation *ref*:

$$RMSESS_{sim,ref} = 1 - \frac{\overline{RMSE_{sim}(t)}}{\overline{RMSE_{ref}(t)}} \tag{3}$$

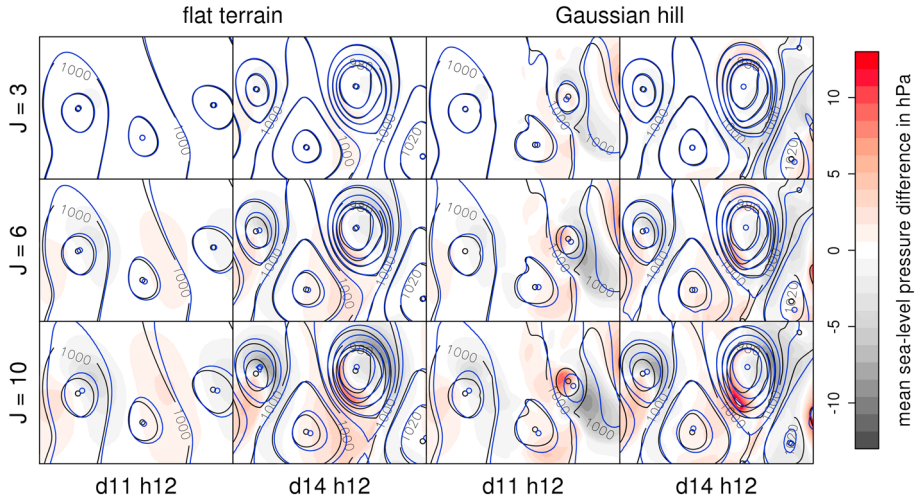

Figure 3. Difference (colors) of mean sea level pressure between *CB* (blue contour lines) and *BB* (black contour lines) over the *LB* domain. Rows show spatial resolution jumps, with flat terrain (first and second columns) and Gaussian hill (third and fourth columns). Two snapshots in time are shown, day 11 hour 12 and day 14 hour 12. *CB* = Coarse Brother; *BB* = Big Brother; *LB* = Little Brother.

When $RMSESS_{sim,ref} > (<) 0$, *sim* has more (less) skill than *ref* and when $RMSESS_{sim,ref} = 0$, they perform similar.

We evaluate (1) *LB* simulations and (2) *CB* and *FB* simulations linearly interpolated between the temporal update times (CB_i and FB_i) to the evaluation time step of 15 min. The latter represent sampling errors due to the linear interpolation at different temporal update frequencies. The reference are *CB* and *FB* simulations, respectively

3. Results and Discussion

3.1. *BB*, *CB*, and *FB* simulations

3.1.1. General Description of the Wave in Reference *BB*

As described in section 2.3.1, the wave was induced by a disturbance in the initial field of a zonal midlatitude jet. Low- and high-pressure systems developed and were visibly pronounced from day 10 over flat terrain, and several days earlier with the Gaussian hill. As mentioned earlier, all simulations covered 17 days and

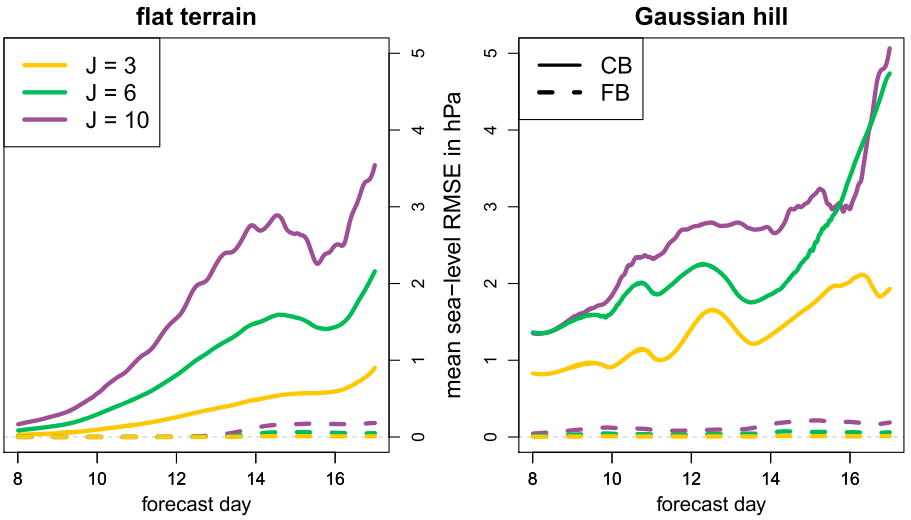

Figure 4. Different driving simulations: RMSE between *CB* and *BB* (solid lines)/*FB* and *BB* (dashed lines) over *LB* domain, flat terrain (left), and with Gaussian hill (right) in hectopascals. Colors indicate the spatial resolution jump. RMSE = root-mean-square error; *CB* = Coarse Brother; *BB* = Big Brother; *FB* = Filtered Brother; *LB* = Little Brother.

Table 2
Temporal Update Frequency and Spatial Resolution Jump: Time Means of Mean Sea Level Pressure RMSEs (Reference = BB Simulation) in Hectopascals

		U			
J	**CB/FB**	**24**	**8**	**4**	**2**
1		0.01	0.06	0.17	0.62
Flat terrain					
Coarse					
3	0.33	0.33	0.35	0.42	0.79
6	0.94	0.98	0.98	1.02	1.28
10	1.70	1.83	1.84	1.86	2.08
Filtered					
3	0.00	0.01	0.06	0.17	0.61
6	0.02	0.02	0.06	0.17	0.61
10	0.06	0.05	0.08	0.17	0.61
Gaussian hill					
1		0.01	0.05	0.19	0.68
Coarse					
3	1.36	1.07	1.22	1.05	1.21
6	2.21	1.88	1.88	1.88	2.06
10	2.59	2.59	2.64	2.65	3.00
Filtered					
3	0.01	0.02	0.06	0.19	0.68
6	0.04	0.11	0.13	0.23	0.69
10	0.13	0.21	0.22	0.28	0.70

Note. LB simulations driven by *BB* (first and eighth rows), *CB* (second to fourth and ninth to eleventh rows), and *FB* (fifth to seventh and twelfth to fourteenth rows). The second column shows the RMSEs of driving simulations *CB* and *FB*, the other columns RMSEs of *LB* simulations. *BB* = Big Brother; *CB* = Coarse Brother; *FB* = Filtered Brother; *LB* = Little Brother.

evaluation was restricted to the last 9 days. Over flat terrain (Figure 1), the pressure systems reached highest (lowest) values of 1,030 hPa (940 hPa), yielding an amplitude of around 45 hPa. The horizontal extent of the wave was about 3,000 km in the south-north direction. In the direction of propagation, from west to east, it had a wavelength of about 3,500 km with a propagation speed of around 50 km/hr. The *LB* domain covered an area just downstream of the area of cyclogenesis. The intensity of the low-pressure systems increased with time.

Figure 2 shows the map plots for the simulation with a Gaussian hill. The hill activated an additional wave, which starts earlier and further to the east than the one induced by the disturbance in the wind field alone over flat topography. The two waves add up to pressure systems with an amplitude of 65 hPa.

3.1.2. Comparison of CB and FB Simulations to BB

The difference of the coarse simulations *CB* and the filtered simulations *FB* to the fine reference simulation *BB* was evaluated over the *LB* domain. Later, the errors of the *LB* simulations can be compared to that of the driving simulations.

Figure 3 shows exemplary mean sea level pressure map plots of differences $MSLP(CB) - MSLP(BB)$ over the *LB* domain. The two snapshots in time show low-pressure systems crossing the *LB* domain. Figure 4 quantifies the differences between *CB* and *BB* with the RMSE as time series over 9 days. The left panels display flat terrain, and the right panels the Gaussian hill. Time means can be found in Table 2.

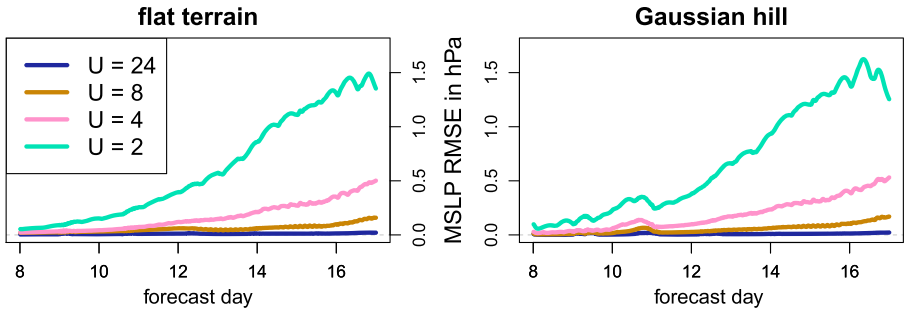

Figure 5. Temporal update frequency: RMSE between *LB* and *BB* over LB domain, flat terrain (left) and Gaussian hill (right) in hectopascals. Colors indicate the temporal update frequency. RMSE = root-mean-square error; *LB* = Little Brother; *BB* = Big Brother; MSLP = mean sea level pressure.

All three coarse simulations *CB* showed similar characteristics, but the errors differ in intensity. Pressure systems generally crossed the domain faster than in *BB*, especially in the first forecast days. Fronts were not as pronounced as in *BB*. This holds for the simulations with flat terrain and with the Gaussian hill (in the latter, however, some additional differences are visible in the vicinity and the wake of the mountain). The mean RMSEs increased with lower resolution and were larger for hill than flat terrain.

The largest errors in the domain were associated with low-pressure systems and fronts (Figure 3), thus, the RMSEs fluctuate with time; starting low and increasing over time as the pressure systems intensified.

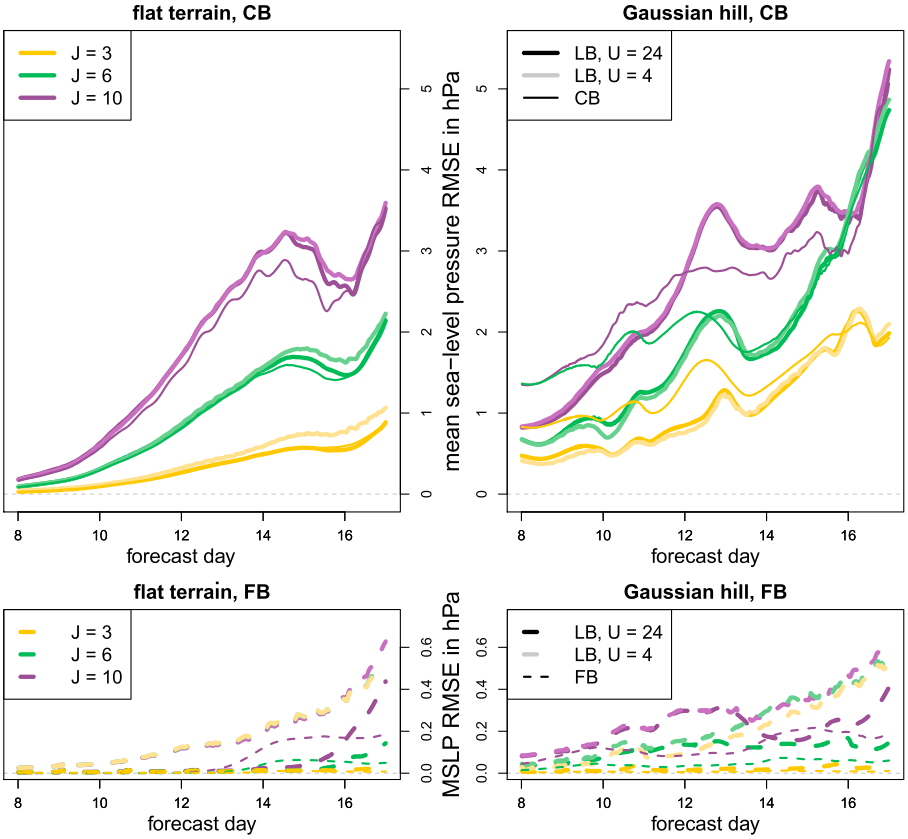

Figure 6. Temporal update frequency and spatial resolution jump: RMSE between *LB* and *BB* in hectopascals, flat terrain (left) and Gaussian hill (right); driven by *CB* (top, solid lines) and *FB* (bottom, dashed lines) for different spatial resolution jumps (colors) and temporal update frequencies $U = 4$ and $U = 24$. The thin lines show the RMSEs of the driving simulations from Figure 4 for comparison. RMSE = root-mean-square error; *LB* = Little Brother; *BB* = Big Brother; *CB* = Coarse Brother; *FB* = Filtered Brother.

Table 3
Temporal Update Frequency and Spatial Resolution Jump: Mean Sea Level Pressure $RMSESS_{sim,ref}$ in Hectopascals of Simulations With Gaussian Hill

		sim : CB_i/FB_i *ref* : *CB*/*FB*					*sim* : *LB ref* : *CB*/*FB*			
	J \ U	**24**	**8**	**4**	**2**	J \ U	**24**	**8**	**4**	**2**
coarse	**3**	0.00	0.00	−0.01	−0.16	**3**	0.21	0.10	0.23	0.11
	6	0.00	0.00	−0.01	−0.07	**6**	0.15	0.15	0.15	0.07
	10	0.00	0.00	−0.01	−0.05	**10**	0.00	−0.02	−0.02	−0.16
filtered	**3**	−1.10	−10.47	−34.44	−105.28	**3**	−1.66	−6.31	−23.51	−88.13
	6	−0.07	−1.18	−5.05	−17.02	**6**	−1.50	−1.86	−4.03	−14.48
	10	−0.01	−0.21	−1.26	−5.29	**10**	−0.63	−0.68	−1.19	−4.45

Note. RMSEs of *LB* simulations with reference *BB* are compared to driving simulations *CB* and *FB*, as are the interpolated data CB_i and FB_i representing sampling errors. *CB* = Coarse Brother; *FB* = Filtered Brother; *LB* = Little Brother.

The Gaussian hill induced the development of pressure systems earlier, resulting in larger RMSEs at the beginning of the evaluation time.

In the filtered simulations *FB*, the problem was narrowed down further, as here the difference in model solutions arising from different grid spacings was excluded. The grid spacing was the same as in *BB*, while the range of represented scales in the simulations was reduced. Thus, the positions of the pressure systems remained unchanged. The baroclinic wave was well resolved by the scales larger than the ones that are cut off, so only smaller features such as fronts and the shape of the low-pressure system center were modified. Hence, the difference between the three *FB* and the reference *BB* simulation were small (Figure 4 and Table 2).

3.2. *LB* Simulations

LB simulations were driven by *BB* (constant $J = 1$ and varying U) and compared to *BB*. Figure 5 shows $RMSE(t)$ for different U and the first and eighth rows in Table 2 the time means. In real RCM simulations, temporal and spatial resolution jumps occur combined. As reported in section 1, typical values are $J = 10$ and $U = 4$.We show *LB* simulations with $U \epsilon (24, 8, 4, 2)$ and $J \epsilon (3, 6, 10)$, where simulations are driven by *CB* and *FB*. Some exemplary time plots are shown in Figure 6, time means of RMSEs are given in Table 2, and RMSESSs for the Gaussian hill case are in Table 3.

3.2.1. Temporal Update Frequency

Big Brother driving data BB. As expected, RMSEs increase with decreasing U. The areas of largest errors are around the low-pressure systems and the fronts, which are generally too weakly represented with low temporal update frequency. The simulations with Gaussian hill introduce an additional inconsistency between *BB* and *LB* as long as the influence of the hill is larger than that of the wave induced by the initial wind field perturbance in the driving data. So in the beginning of the evaluation period, errors are slightly higher (Figure 5). Later, the flow is dominated by the driving data and the errors align with those without the hill. In the simulations with Gaussian hill, the *LB* simulations can counteract the sampling error of the driving data, as the RMSEs for BB_i are 0.01 / 0.09 / 0.27 / 0.81 for $U = 24 / 8 / 4 / 2$, larger than the errors of *LB* (Table 2, first and eighth rows).

Coarse driving data CB. Both with flat terrain and Gaussian hill, RMSEs at $U = 2$ (LBC update every 12 hr) are large in comparison to $U > 2$ (Table 2). The 12-hourly update is not able to sufficiently transfer the information of the passing pressure systems from the *CB* to the *LB*, which is also evident in the skill scores of the interpolated CB_i data compared to *CB* (Table 3, top left block). Skill scores are negative for $U = 2$, and approximately 0 for $U > 2$. Overall, an update frequency of $U = 4$ appears to be sufficient for larger spatial resolution jumps ($J \geq 6$), as then the error is explained by the *CB* error and increasing the temporal update frequency does not help. At $J = 3$, however, a temporal update of 3 hr ($U = 8$) seems to be superior to 6-hourly ($U = 4$), coinciding with the estimate for the largest acceptable nesting time interval by Matte et al. (2017). Constraining the *LB* with "wrong" *CB* boundary data in a higher frequency does not improve the simulations.

Filtered driving data FB. Here, as already mentioned, the positions of the pressure systems are correct in the *FB* simulations, resulting in overall much smaller errors than in the simulations driven by *CB*. Varying U has a strong influence on the RMSE in the *LB* simulations. With the Gaussian hill, again, errors are larger than those of the driving simulations *FB*. *RMSESS* reach large values (Table 3, bottom row), as the reference errors are very small. Still, in the Gaussian hill case, LB simulations can counteract the sampling error n the majority of cases, when the *MSESS* of *LB* are smaller than those of FB_i As, however, the errors of *LB* simulations are multiple times larger than those of the driving *FB* simulations at $U \leq 4$, a 3-hourly boundary update ($U = 8$) seems reasonable.

3.2.2. Spatial Resolution Jump

Coarse driving data CB. The error becomes larger with increasing J, following the error of the *CB* driving data (Figure 6). Especially in the simulations with the Gaussian hill, the added value of the nested model is visible. The errors of *LB* compared to *BB* are smaller than the ones of *CB* ($RMSESS_{LB,CB} > 0$; see Table 3, top right block) for $J < 10$, but for $J = 10$ they are the same ($U = 24$) or larger ($U < 24$). This indicates that the nested *LB* simulations can produce features lacking in the *CB* simulations, mainly in the first half of the evaluation time when the influence of the hill is stronger than that of the pressure systems induced by the wind perturbance in the driving simulations. The *LB* simulations can recover the flow downstream of the hill, by using the correct high-resolved topography, although it is represented deficiently in the *CB* driving data due to smoothed topography.

Filtered driving data FB. With flat terrain, the influence of varying J is minimal compared to that of varying U. With the Gaussian hill, a weak dependency on J is visible which is stronger for increasing U.

3.2.3. Different LBC Schemes DR and ME

The exemplary simulations that have been performed with Mesinger Eta-model LBCs perform similarly to that with DR. RMSEs are sometimes smaller and sometimes larger for ME than for DR, but the differences are small. Consequently, the use of ME should be considered, especially since DR has the inherent disadvantage over ME of being computationally more costly, as more data at the boundary cannot be used for evaluation.

3.2.4. Spectral nudging

Simulations with spectral nudging perform similar to those without. The data used for nudging is the *CB* and *FB* data, which differs from the "true" reference data *BB*. Thus, the regional fields are nudged toward the wrong solution and spectral nudging has no beneficial effect.

4. Conclusions

In this paper, we investigated the errors arising from the choices with regard to the lateral boundary conditions when using a LAM. We used an idealized experiment setting in the Big-Brother-Experiment framework. For this, the baroclinic wave test case on the f plane in a dry atmosphere was implemented in the RCM COSMO-CLM. It was used for producing driving data for nested simulations: reference simulation *BB*, coarse *CB* simulations independent of *BB*, and filtered driving simulations *FB*. An alternative LBC scheme (Mesinger Eta-model LBCs, ME) was successfully adapted to the Arakawa C-grid and implemented in COSMO-CLM. Different nesting strategies were tested by varying the LBC formulation (ME or DR), temporal update frequencies and spatial resolution jumps, and the use of spectral nudging. We answer the three questions that were raised in the introduction:

1. For temporal update frequency, $U = 4$ (6-hourly) is the suggested lower limit. Less frequent lateral boundary updates resulted in insufficient representation of the synoptic-scale phenomena at the lateral boundaries, but updates more often did not reduce errors considerably. The use of 3-hourly ($U = 8$) boundary data improved the simulations only when errors are low (i.e., the simulations driven by *FB*), otherwise, erroneous boundary data (i.e., *CB*) prescribed too often is detrimental to the *LB* simulation.
   With coarse *CB*, the errors in the driving data dominated the nesting errors in *LB* simulations. Errors increased with larger J, explained by the decreasing quality of the *CB* driving data. In the case with Gaussian hill, the *LB* was able to reduce errors when $J \leq 6$. With *FB*, *LB* simulations with all spatial resolution jumps $J \leq 10$ performed similar, as the synoptic-scale baroclinic wave was sufficiently represented in the filtered driving data.

2. In the idealized simulations of the synoptic-scale baroclinic wave, no clear advantage of either of the two LBC schemes could be seen. ME, however, has the advantage of having a smaller boundary zone, thus needing less computational resources.
3. In these idealized experiments, there was no benefit of applying spectral nudging, as it imprinted the driving models deficits on the nested simulations driven by *CB*. With *FB* driving data, the inconsistencies at the boundaries are small anyway, so that spectral nudging had a very small effect.

Over flat terrain, the performance of *LB* simulations was close to that of the driving *CB* and *FB* simulations. The beneficial effect of a LAM with higher resolution was visible in the case with Gaussian hill. Here, due to the better representation of processes downstream of the hill, the *LB* simulations were closer to the reference *BB* than the driving simulations *CB*. The nested simulations were strongly dependent on the quality of the driving data and insensitive to the two LBC scheme. It should be considered to use the ME LBC scheme, as it performs similar to the widely used DR and is computationally less demanding. Although driving data with high temporal resolution are available (e.g., ECMWF ERA5 reanalysis, Hersbach et al., 2018), for downscaling to grid spacings of about 10 km, from our experiments we recommend 6-hourly lateral boundary updates and spatial resolution jumps of up to 6.

Even here in these idealized experiments, the benefit of downscaling and the impact of nesting strategy was noticeable. For more robust statements and expanding the investigations to regional climate modeling, especially regarding the LBC scheme and the validity of previous recommendations of temporal and spatial resolution jumps for models with higher resolution, more experiments should be conducted, for example, at the convection permitting scale, which is used more and more in RCMs and where LBCs have not been investigated systematically yet. A next step could consequently be a test with improved representation of small-scale physics, clouds, and precipitation instead of the synoptic-scale baroclinic wave, to include other known sources of added value of an RCM, next to the better representation of topography as here the Gaussian hill. We expect larger inconsistencies between driving data and RCM simulation, resulting in larger sensitivity to the nesting strategy.

Appendix A: Discrete Cosine Transform Filter

Filtering is done with the technique presented in Denis, Côté, and Laprise (2002). The 2-D fields on all model levels of the Big Brother (*BB*) variables which are necessary for boundary input for the Little Brother (*LB*) are transformed to spectral space with the discrete cosine transform. Then, wavelengths below a certain threshold are filtered by a transfer function to represent a coarser model solution. Figure A1 shows the transfer functions for three different resolution jumps which are squared cosines. The transfer function is 0 below the threshold wavelength $\lambda_{\min}$, 1 above $\lambda_{\max} = 2\lambda_{\min}$, and a squared cosine in between. The cutoff wavelength is set to the approximate resolution of a corresponding coarse Brother simulations with resolution jump J: $\lambda_{\min} = J \times 2 \times$ *grid distance LB* (values in Table A1). Finally, the data are transformed back to physical space with the inverse discrete cosine transform, and these filtered Brother data are still given on the high-resolution *BB* grid.

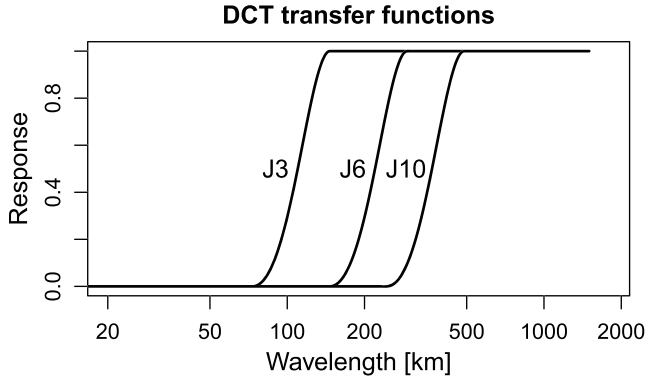

Figure A1. Transfer functions for the discrete cosine transform filter to generate *FB* from *BB*. DCT = discrete cosine transform. *FB* = Filtered Brother; *BB* = Big Brother.

Table A1
Threshold Wavelengths Defining the Transfer Functions for the Discrete Cosine Transform Filter to Generate FB From BB

J	λ_{min}	λ_{max}
3	73.26 km	146.52 km
6	146.52 km	293.04 km
10	244.20 km	488.40 km

Note. *FB* = Filtered Brother; *BB* = Big Brother.

Acknowledgments
We thank the Deutscher Wetterdienst (DWD) for providing computational facilities at the DMRZ (Deutsches Meteorologisches Klimarechenzentrum). This work was carried out in the framework of the German research project MiKlip II: Regionalisation (FKZ 01LP1518C), funded by the German Federal Ministry of Education and Research (BMBF). COSMO-CLM is the community model of the German regional climate research, which is available for community members at the website (https://www.clm-community.eu). Namelists for reproducing the simulations and the data used for evaluation is available online: (DOI 10.5281/zenodo.2671698). We thank the two reviewers for their proficient reviews and helpful comments.

References

Antic, S., Laprise, R., Denis, B., & de Elía, R. (2006). Testing the downscaling ability of a one-way nested regional climate model in regions of complex topography. *Climate Dynamics*, *26*(2), 305–325. https://doi.org/10.1007/s00382-005-0046-z

Beck, A., Ahrens, B., & Stadlbacher, K. (2004). Impact of nesting strategies in dynamical downscaling of reanalysis data. *Geophysical Research Letters*, *31*, L19101. https://doi.org/10.1029/2004GL020115

Becker, N., Ulbrich, U., & Rupert, K. (2015). Systematic large-scale secondary circulations in a regional climate model. *Geophysical Research Letters*, *42*, 4142–4149. https://doi.org/10.1002/2015GL063955

Black, T. L. (1988). *The Step-Mountain, Eta Coordinate Model: A documentation*. Washington, DC: NOAA/NWS National Meteorological Center. April 1988, with revisions later.

Blahak, U. (2015). Simulating idealized cases with the COSMO-model (draft version).

Brisson, E., Demuzere, M., & van Lipzig, N. P. M. (2015). Modelling strategies for performing convection-permitting climate simulations. *Meteorologische Zeitschrift*, *25*(2), 149–163. https://doi.org/10.1127/metz/2015/0598

Davies, H. C. (1976). A lateral boundary formulation for multi-level prediction models. *Quarterly Journal of the Royal Meteorological Society*, *102*(432), 405–418. https://doi.org/10.1002/qj.49710243210

Denis, B., Côté, J., & Laprise, R. (2002). Spectral decomposition of two-dimensional atmospheric fields on limited-area domains using the discrete cosine transform (DCT). *Monthly Weather Review*, *130*(7), 1812–1829. https://doi.org/10.1175/1520-0493(2002)130<1812:SDOTDA>2.0.CO;2

Denis, B., Laprise, R., & Caya, D. (2003). Sensitivity of a regional climate model to the resolution of the lateral boundary conditions. *Climate Dynamics*, *20*(2), 107–126. https://doi.org/10.1007/s00382-002-0264-6

Denis, B., Laprise, R., Caya, D., & Côté, J. (2002). Downscaling ability of one-way nested regional climate models: The Big-Brother Experiment. *Climate Dynamics*, *18*(8), 627–646. https://doi.org/10.1007/s00382-001-0201-0

Doms, G., & Baldauf, M. (2015). A description of the nonhydrostatic regional COSMO-model part I: Dynamics and numerics [Computer software manual]. Offenbach, Germany.

Giorgi, F., Jones, C., & Ghassem, R. A. (2009). Addressing climate information needs at the regional level: The CORDEX framework (Vol. 58; Tech. Rep. No. 3). Geneva, Switzerland: WMO bulletin.

Giorgi, F., & Mearns, L. O. (1999). Introduction to special section: Regional climate modeling revisited. *Journal of Geophysical Research*, *104*(D6), 6335–6352. https://doi.org/10.1029/98JD02072

Hargreaves, J. C. (2010). Skill and uncertainty in climate models. *Wiley Interdisciplinary Reviews: Climate Change*, *1*(4), 556–564. https://doi.org/10.1002/wcc.58

Hersbach, H., de Rosnay, P., Bell, B., Schepers, D., Simmons, A., Soci, C., et al. (2018). Operational global reanalysis: Progress, future directions and synergies with NWP (*Tech. Rep. No. 27*). Reading, United Kingdom: European Centre for Medium-Range Weather Forecast, ERA Report Series.

Jablonowski, C., & Williamson, D. L. (2006). A baroclinic instability test case for atmospheric model dynamical cores. *Quarterly Journal of the Royal Meteorological Society*, *132*(621C), 2943–2975. https://doi.org/10.1256/qj.06.12

Køltzow, M., Iversen, T., & Haugen, J. E. (2008). Extended Big-Brother experiments: The role of lateral boundary data quality and size of integration domain in regional climate modelling. *Tellus A*, *60*(3), 398–410. https://doi.org/10.1111/j.1600-0870.2008.00309.x

Marbaix, P., Gallée, H., Brasseur, O., & van Ypersele, J.-P. (2003). Lateral boundary conditions in regional climate models: A detailed study of the relaxation procedure. *Monthly Weather Review*, *131*(3), 461–479. https://doi.org/10.1175/1520-0493(2003)131<0461:LBCIRC>2.0.CO;2

Matte, D., Laprise, R., Thériault, J. M., & Philippe, L.-P. (2017). Spatial spin-up of fine scales in a regional climate model simulation driven by low-resolution boundary conditions. *Climate Dynamics*, *49*(1), 563–574. https://doi.org/10.1007/s00382-016-3358-2

McDonald, A (1999). A review of lateral boundary conditions for limited area forecast models. *Proceedings of the Indian National Science Academy. Part A. Physical Sciences*, *65*, 91–105.

McDonald, A. (2002). A step toward transparent boundary conditions for meteorological models. *Monthly Weather Review*, *130*(1), 140–151. https://doi.org/10.1175/1520-0493(2002)130<0140:ASTTBC>2.0.CO;2

Mesinger, F. (1977). Forward-backward scheme, and its use in a limited area model. *Beiträge zur Physik der Atmosphäre*, *50*, 200–210.

Mesinger, F., & Veljovic, K. (2013). Limited area NWP and regional climate modeling: A test of the relaxation vs Eta lateral boundary conditions. *Meteorology and Atmospheric Physics*, *119*(1), 1–16. https://doi.org/10.1007/s00703-012-0217-5

Mesinger, F., & Veljovic, K. (2017). Eta vs. sigma: Review of past results, Gallus–Klemp test, and large-scale wind skill in ensemble experiments. *Meteorology and Atmospheric Physics*, *129*(6), 573–593. https://doi.org/10.1007/s00703-016-0496-3

Mieruch, S., Feldmann, H., Schädler, G., Lenz, C.-J., Kothe, S., & Kottmeier, C. (2014). The regional MiKlip decadal forecast ensemble for Europe: The added value of downscaling. *Geoscientific Model Development*, *7*(6), 2983–2999. https://doi.org/10.5194/gmd-7-2983-2014

Nordström, J. (2017). A roadmap to well posed and stable problems in computational physics. *Journal of Scientific Computing*, *71*, 365–385. https://doi.org/10.1007/s10915-016-0303-9

Omrani, H., Drobinski, P., & Dubos, T. (2012). Optimal nudging strategies in regional climate modelling: Investigation in a Big-Brother experiment over the European and Mediterranean regions. *Climate Dynamics*, *41*, 2451–2470. https://doi.org/10.1007/s00382-012-1615-6

Orlanski, I. (1975). A rational subdivision of scales for atmospheric processes. *Bulletin of the American Meteorological Society*, *56*, 527–534.
Paeth, H., & Mannig, B. (2013). On the added value of regional climate modeling in climate change assessment. *Climate Dynamics*, *41*(3), 1057–1066. https://doi.org/10.1007/s00382-012-1517-7
Pham, T. V., Brauch, J., Früh, B., & Ahrens, B. (2018). Added decadal prediction skill with the coupled regional climate model COSMO-CLM/NEMO. *Meteorologische Zeitschrift*, *27*(5), 391–399. https://doi.org/10.1127/metz/2018/0872
Räisänen, J. (2007). How reliable are climate models? *Tellus, Series A: Dynamic Meteorology and Oceanography*, *59*(1), 2–29. https://doi.org/10.1111/j.1600-0870.2006.00211.x
Roberts, M. J., Vidale, P. L., Senior, C., Hewitt, H. T., Bates, C., Berthou, S., et al. (2018). The benefits of global high-resolution for climate simulation: Process-understanding and the enabling of stakeholder decisions at the regional scale. *Bulletin of the American Meteorological Society*, *99*(11), 2341–2359. https://doi.org/10.1175/BAMS-D-15-00320.1
Rockel, B., Will, A., & Hense, A. (2008). The regional climate model COSMO-CLM (CCLM). *Meteorologische Zeitschrift*, *17*(4), 347–348. https://doi.org/10.1127/0941-2948/2008/0309
Rummukainen, M. (2010). State-of-the-art with regional climate models. *Wiley Interdisciplinary Reviews: Climate Change*, *1*(1), 82–96. https://doi.org/10.1002/wcc.8
Schättler, U., Doms, G., & Schraff, C. (2016). A description of the nonhydrostatic regional COSMO-model Part VII: User's guide [Computer software manual]. Offenbach, Germany.
Sundström, A. (1973). Theoretical and practical problems in formulating boundary conditions for a limited-area model (*Tech. Rep. No. DM-9*). Stockholm, Sweden: University of Stockholm, Department of Meteorology.
Taylor, K. E., Stouffer, R. J., & Meehl, G. A. (2012). An overview of CMIP5 and the experiment design. *Bulletin of the American Meteorological Society*, *93*(4), 485–498. https://doi.org/10.1175/BAMS-D-11-00094.1
Ullrich, P. A., Reed, K. A., & Jablonowski, C. (2015). Analytical initial conditions and an analysis of baroclinic instability waves in f- and β-plane 3D channel models. *Quarterly Journal of the Royal Meteorological Society*, *141*(693), 2972–2988. https://doi.org/10.1002/qj.2583
Veljovic, K., Rajkovic, B., Fennessy, M. J., Altshuler, E. L., & Mesinger, F. (2010). Regional climate modeling: Should one attempt improving the large scales? Lateral boundary condition scheme: Any impact? *Meteorologische Zeitschrift*, *19*(3), 237–246. https://doi.org/10.1127/0941-2948/2010/0460
von Storch, H., Langenberg, H., & Feser, F. (2000). A spectral nudging technique for dynamical downscaling purposes. *Monthly Weather Review*, *128*(10), 3664–3673. https://doi.org/10.1175/1520-0493(2000)128<3664:ASNTFD>2.0.CO;2
Warner, T. T., Peterson, R. A., & Treadon, R. E. (1997). A tutorial on lateral boundary conditions as a basic and potentially serious limitation to regional numerical weather prediction. *Bulletin of the American Meteorological Society*, *78*(11), 2599–2618. https://doi.org/10.1175/1520-0477(1997)078<2599:ATOLBC>2.0.CO;2